

Article

# Experimental and Numerical Analysis of the Effect of Vortex Generator Height on Vortex Characteristics and Airfoil Aerodynamic Performance

Xinkai Li <sup>1,2,3,\*</sup> , Ke Yang <sup>1,2,3,4</sup> and Xiaodong Wang <sup>5</sup><sup>1</sup> Institute of Engineering Thermophysics, Chinese Academy of Sciences, Beijing 100190, China; yangke@iet.cn<sup>2</sup> Key Laboratory of Wind Energy Utilization, Chinese Academy of Sciences, Beijing 100190, China<sup>3</sup> Dalian National Laboratory for Clean Energy, CAS, Beijing 100190, China<sup>4</sup> Graduate School, University of Chinese Academy of Sciences, Beijing 100049, China<sup>5</sup> College of Energy, Power and Mechanical Engineering, North China Electric Power University, Beijing 102206, China; wangxd@ncepu.edu.cn

\* Correspondence: lixinkai@iet.cn; Tel.: +86-010-8254-3038

Received: 29 January 2019; Accepted: 7 March 2019; Published: 12 March 2019



**Abstract:** To explore the effect of the height of vortex generators (VGs) on the control effect of boundary-layer flow, the vortex characteristics of a plate and the aerodynamic characteristics of an airfoil for VGs were studied by both wind tunnel experiments and numerical methods. Firstly, the ratio of VG height ( $H$ ) to boundary layer thickness ( $\delta$ ) was studied on a flat plate boundary layer; the values of  $H$  are  $0.1\delta$ ,  $0.2\delta$ ,  $0.5\delta$ ,  $1.0\delta$ ,  $1.5\delta$ , and  $2.0\delta$ . Results show that the concentrated vortex intensity and VG height present a logarithmic relationship, and vortex intensity is proportional to the average kinetic energy of the fluid in the height range of the VG. Secondly, the effects of height on the aerodynamic performance of airfoils were studied in a wind tunnel using three VGs with  $H = 0.66\delta$ ,  $1.0\delta$ , and  $1.33\delta$ . The stall angle of the airfoil with and without VGs is  $18^\circ$  and  $8^\circ$ , respectively, so the VGs increase the stall angle by  $10^\circ$ . The maximum lift coefficient of the airfoil with VGs increases by 48.7% compared with the airfoil without VGs, and the drag coefficient of the airfoil with VGs is 84.9% lower than that of the airfoil without VGs at an angle of attack of  $18^\circ$ . The maximum lift–drag ratio of the airfoil with VGs is lower than that of the airfoil without VGs, so the VGs do not affect the maximum lift–drag ratio of the airfoil. However, a VG does increase the angle of attack of the best lift–drag ratio.

**Keywords:** vortex generators; wind turbine; airfoil; aerodynamic performance

## 1. Introduction

According to the latest data from the Global Wind Energy Council [1], as of 2017, the total installed capacity of the global wind power market has reached 539.6 GW, and wind power has become the third largest power source in the world. However, during the operation of wind turbines, the blade root is prone to flow separation, which decreases the power of wind turbines [2–6]. Many novel methods have been proposed for improving the performance of wind turbine blades in recent years, such as vortex generators (VGs) [7], microflaps [8], microtabs [4], blowing and suction [9], synthetic jets [10], flexible wall [11], and plasma actuators [12]. A comparison of these methods was performed by Barlas [13] and Johnson [14] to illustrate their efficiency. As reported by Lin [7] and Wang [15], vortex generators are among the most effective devices for improving the aerodynamic performance of blades.

Taylor [16] introduced vortex generators in 1947, and they were originally implemented in the field of flow control for aircraft wings. The principle underlying VGs' control of flow separation is that when a fluid flows over VGs, a concentrated vorticity is generated. Under the action of the

concentrated vortices, the high-energy fluid outside the boundary layer will be drawn into the bottom of the boundary layer, and energy will be injected into the low-energy fluid in the boundary layer, thus delaying the separation of the boundary layer [17,18]. Abdollah [19] used a numerical simulation method to verify whether installing VGs on wind turbine blades increases the efficiency of the wind turbine. Because of their simple structure and convenient installation, VGs have been widely utilized in the field of flow control [20–22] and heat transfer [23,24]. Lin [7] studied the mechanism by which VGs control the flow separation in the boundary layer on a flat plate by using an experimental method. Godard [25–27] studied the effect of a triangular VG arrangement on the control of boundary-layer separation with an inverse pressure gradient by an experimental method. Urkiola et al. [22] described the vortex characteristics of a single VG on the basis of a Computational Fluid Dynamics (CFD) method. Velte et al. [28] measured the flow field of a rectangular VG on a flat plate; in their experiment, the VG height was the thickness of the local flat plate boundary layer. The relationships between the installation angle of the VGs and the radius of the vortex core, vortex circulation, and the induced velocity of the vortex core were studied by varying the installation angle of the VGs in the range of  $20^\circ \leq \beta \leq 40^\circ$ . The results demonstrated that these quantities change linearly with the change in the installation angle of the VGs. It was also found that, although the VG is located in the turbulent boundary layer, the induced vortices are stable. Angele and Grewe [29] studied the control method of turbulent boundary-layer separation, and the transient eddy behavior of the turbulent boundary layer was analyzed in detail. To research airfoil flow separation control, Sørensen et al. [30] described a CFD procedure that can handle a geometrical resolved VG on an airfoil section. The airfoils of FFA-W3-301 and FFA-W3-360 were taken as the research objects. The results of calculation were compared with those of wind tunnel experiments. This method cannot accurately capture the details of a VG's flow field, but it can be used to qualitatively compare the effects of different VG parameters on the flow field. Mueller-Vahl et al. [31] studied the effect of chordwise position, spanwise spacing, and VG size on the aerodynamic characteristics of an airfoil by using force balance measurements for a 2D airfoil section. Wang et al. [15] investigated the influence of double-row VGs on the aerodynamic characteristics of the airfoil, and the development law of vortices along the flow direction was analyzed. The results showed that double-row VGs can effectively improve the lift coefficient of the airfoil and control airflow separation, which has a definite guiding significance for the application of VGs in wind turbine blades. The DU97-W-300 airfoil was adopted by Gao et al. [18] to study the effects of different combinations of VGs on the aerodynamic characteristics of an airfoil using a numerical method. Fouatih et al. [32] used an experimental method to study the effect of vortex generators on flow separation of the NACA 4415 airfoil, and they optimized the vortex generator's geometric parameters, including the installation position and installation angle. Velte and Hansen [33] carried out a three-dimensional particle image velocimetry for the DU91-w2-250 airfoil in a wind tunnel, and the impact of the VGs on the flow near stall was studied. The flow structures induced by the VGs and the separation-controlling effects on the airfoil were investigated in detail.

Hansen et al. [34] presented a VG aerodynamic configuration that can provide airfoils with a higher lift–drag ratio. The maximum lift of an airfoil reached 1.82, and the maximum lift–drag ratio increased from 110 to 114.5 by using this configuration of VGs. Kerho et al. [35] experimentally studied the effects of several VG structures on the aerodynamic performance of airfoils. The results demonstrated that for an airfoil with leading separation bubbles, the separation can be effectively controlled by installing VGs in the positions before the separation bubbles and after the peak pressure of the suction surface of the airfoil. Delft University also conducted relevant experimental studies on DU series airfoil sections [36]. The vortex generator was installed at  $0.2c$  from the leading edge. The results showed that the maximum lift coefficient increased from 1.55 to 1.97, and the drag coefficient increased before the stall angle and decreased after the stall angle. In addition to the above reports, the application of VGs in wind turbines is further discussed. Gyatt [37] analyzed and experimentally studied a small two-blade horizontal-axis wind turbine (diameter of 9.75 m) equipped with reverse-placement VGs. The arrangement of VGs can be divided into three types: inside half-blade spanwise, outside half-blade

spanwise, and whole blade spanwise. Field measurements showed that the power of wind turbine blades with VGs increased by 20% when the wind speed was greater than 10 m/s, and when the wind speed was low, the reduction in the power was less than 4%. The results also showed that VGs should be installed in the outside half-blade spanwise. Sullivan [38] carried out wind farm measurements on the power and structural dynamic loads of a 2.5 MW horizontal-axis wind turbine blade with VGs. The results showed that the annual power could be increased by 20% when the VGs were installed at positions ranging from 20 to 100% of the blade spanwise, and the annual power could be increased by about 10% by arranging VGs in the 20–70% blade spanwise range. To solve the problem of the drag increasing as the lift increases in a rectangular arrangement of plate VGs, Kogaki et al. [28] adopted the airfoil VG, which not only ensures the function of VGs but also does not reduce the lift–drag ratio. However, this result can only be applied to small wind turbine blades with a low Reynolds number. Afjeh et al. [39] used lift line theory to simulate the flow around the blades, and the mirror eddy method was applied to study the effect of flow vortices generated by VGs on the flow around the blades. A fast calculation method for the aerodynamic characteristics of a horizontal-axis wind turbine with VGs was established and compared with the measured wind power of MOD-2, and the results showed that the method is feasible.

Although many scholars have studied the flow control mechanism of VGs, there are still many scientific problems related to the application of VGs for the flow control of wind turbine blades. For example, the optimum VG height to realize the best flow control effect has not been determined. Vortex generator height is often related to the local boundary layer thickness; the influence of the ratio of VG height to boundary layer thickness on the vorticity characteristics, as well as the influence of VG height on the lift and drag characteristics of airfoils, has not been reported yet. In this study, numerical simulation methods were used to study the influence of the VG height to boundary layer thickness ratio on the vortices' characteristics on a flat plate, and the influence of VG height on the aerodynamic characteristics of wind turbine airfoils was investigated in a wind tunnel.

## 2. Methods

### 2.1. Numerical Conditions

Fluent software was adopted for steady numerical calculations. The finite volume method was used for the discretization of the Navier–Stokes (N–S) equation with the second-order accuracy central difference scheme for spatial discretization, and the pressure–velocity coupling algorithm SIMPLE was adopted. The full-turbulence Spalart–Allmaras (S–A) model was selected as the turbulence model. The mesh of the computational domain was divided using ICEM software: 80 mesh nodes were arranged in the height and chord direction of the VG, and 200 mesh nodes were arranged downstream of the VG. The total number of mesh nodes was about 5,000,000. The height of the first layer near the VG was set to  $1.2 \times 10^{-5}$  mm, with the wall  $y^+$  less than 1 over the VG surface. The mesh distribution on the surface and bottom of the VG is shown in Figure 1.

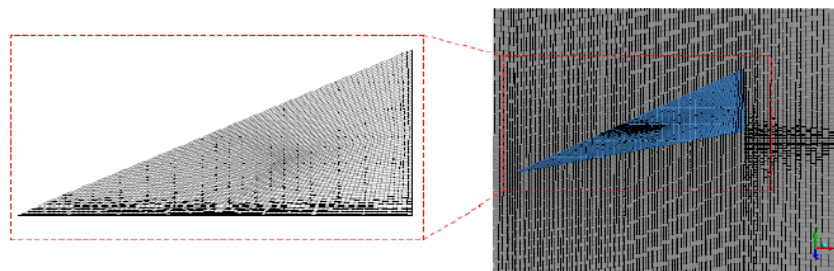


Figure 1. Computational mesh.

In order to observe the motion of vortices developed downstream of the VG, the computational domain was set to  $144H$  (where  $H$  is the height of the VG), and the VG was set to  $9H$  away from the

inlet. The width and height of the computational domain were  $20H$ . The boundary conditions included the velocity inlet, pressure outlet, symmetrical boundary on both sides of the computational domain, free outflow boundary condition on the upper boundary, and non-sliding solid wall on the bottom and VG. The computational domain and boundary conditions are shown in Figure 2.

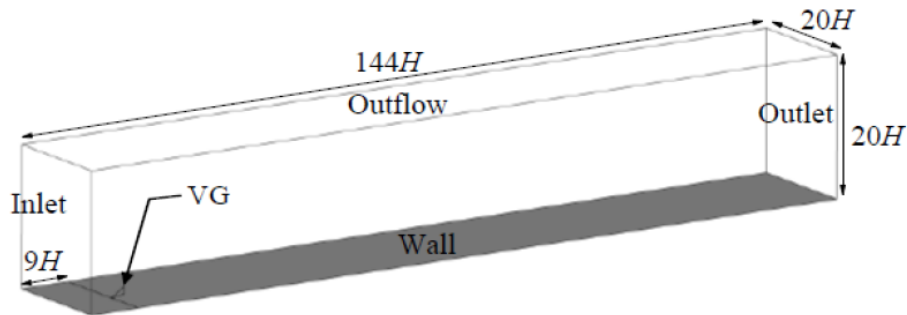


Figure 2. Computational domain and boundary conditions.

The boundary layer often presents a turbulent form for VGs; therefore, this paper mainly studies the vortices' characteristics for VGs with different turbulent boundary layer heights. Changing the height of the VG ( $H$ ) means altering the height of  $h/\delta$  (as shown in Figure 3). Therefore, the purpose of studying VG height was achieved by changing the boundary layer height of the velocity type of the turbulence at the inlet. The inlet turbulence velocity type is given as follows:

$$u = \begin{cases} U(\frac{y}{\delta})^{1/7} & y < \delta \\ U & y \geq \delta \end{cases} \quad (1)$$

where  $u$  is the local velocity,  $\delta$  is the thickness of the boundary layer,  $U$  is the main velocity, and  $y$  is the normal height of the wall.

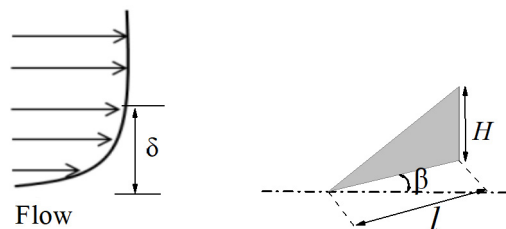


Figure 3. Diagram of VG height ( $H$ ) and boundary layer thickness ( $\delta$ ).

Table 1 shows the geometric parameters of the VG. The VG was set as a wall without thickness. Inflow velocity was  $U = 82$  m/s, and the Reynolds number based on VG height was about  $3 \times 10^4$ . Table 2 shows the ratio of VG Height to Different Boundary Layer (BL) Thickness.

Table 1. VG geometric parameters.

Setting Angle $\beta$ ( $^\circ$ )	Length $l$ (mm)	Hight $H$ (mm)
20	17	5

**Table 2.** Ratio of VG Height to Different BL Thickness.

Height Ratio	Case 1	Case 2	Case 3	Case 4	Case 5	Case 6
$H/\delta$	0.1	0.2	0.5	1.0	1.5	2.0
$H/\delta^*$	0.717	1.295	2.475	3.521	4.032	4.347
$H/\theta$	1.03	2.083	5.15	10.416	15.479	20.661

$\delta$  (BL Thickness),  $\delta^*$  (displacement thickness),  $\theta$  (momentum thickness).

Equations (2) and (3) were used to define the lift and drag coefficients of the VG, respectively:

$$C_l = \frac{F_l}{\frac{1}{2}\rho V_\infty^2 L} \quad (2)$$

$$C_d = \frac{F_d}{\frac{1}{2}\rho V_\infty^2 L} \quad (3)$$

where  $F_l$  and  $F_d$  are the total lift and drag forces of VG;  $\rho$  is the air density, and  $\rho = 1.225 \text{ kg/m}^3$ ;  $V_\infty$  is the free stream velocity of the VG,  $V_\infty = 82 \text{ m/s}$ ;  $L$  is the bottom chord length of the VG,  $L = 17 \text{ mm}$ . In order to prove the adequacy of the grid resolution, grid-independent computation was carried out. Three sets of grids with different densities were calculated: 2,560,000 (coarse), 3,645,000 (medium), and 500,000 (fine). In addition, the Richardson extrapolation method [40] was used to verify the validity of the grid resolution. Table 3 shows the result of Richardson extrapolation. The calculation case is  $H = 1.0\delta$ . In the table,  $C_l$ ,  $C_d$ , and  $C_l/C_d$  are the results for the different grid densities, respectively. RE is the value obtained by Richardson extrapolation,  $R$  is the ratio of errors, and  $p$  is the order of accuracy. The convergence conditions are  $0 < R < 1$  (monotonic convergence);  $R < 0$  (oscillation convergence); and  $1 < R$  (divergence). Since all the calculated results for  $R$  are less than 1, the mesh computation is monotonically convergent. Therefore, the fine grid was used for the presented computations.

**Table 3.** Results of the grid independence study.

Variables	Mesh			Richardson Extrapolation		
	Coarse	Medium	Fine	RE	$p$	$R$
$C_l$	0.5893	0.5918	0.5921	0.5922	3.05	0.12
$C_d$	0.2237	0.225	0.2251	0.2251	3.70	0.07
$C_l/C_d$	2.6211	2.6219	2.6221	2.6222	2.0	0.25

## 2.2. Experiment Setup

The experiment was conducted in the wind tunnel of North China Electric Power University (NCEPU), and the wind tunnel is a large closed return wind tunnel. The airfoil was tested in a 2-D measurement section with dimensions of  $1.5 \times 3 \times 4.5 \text{ m}^3$ . The maximum wind speed was 62 m/s. The measurement section was equipped with an electronic scanning valve of 256 channels and 64 channels, a PXI data acquisition system, etc. Upstream of the airfoil fitted with a Pitot tube, the total pressure of the inlet pipe was measured according to the Pitot tube principle. The side wall of the Pitot tube pipe had small holes, which were used to measure the static pressure of the upstream flow. Installed in the middle section of the airfoil surface were 96 pressure taps, which were used to measure the pressure coefficient distribution on the airfoil surface. The measuring accuracy is five ten thousandths. The  $C_p$  curve is the average result of time; the time interval is 0.1 second, and 10 seconds was used for sample time-averaging. Downstream of the airfoil, there were 111 total pressure measuring holes and 5 static pressure measuring holes (called the wake rake) that are used to calculate the airfoil drag coefficient. The wind tunnel measurement section and test airfoil are shown in Figure 4.

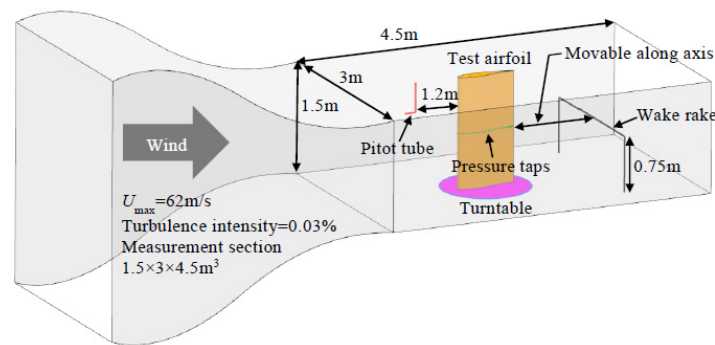


Figure 4. Wind tunnel measurement section size and test airfoil.

The DU93-W-210 airfoil was adopted for the test; the relative thickness of the airfoil is 21%; the chord length ( $C$ ) is 0.8 m; the span of the airfoil is 1.5 m. The DU93-W-210 airfoil is a special airfoil for wind turbines and was developed and designed by Delft University. It is usually arranged at 70% of the blade’s outward span. Depending on the blade length, the actual flow conditions of the airfoil are different, but the optimum operating angle of attack is generally between  $4^\circ$  and  $6^\circ$ . The VGs were located at  $0.2C$  from the leading edge. The test airfoil with VGs is illustrated in Figure 5. The arrangement and height of the VGs are presented in Figure 6, and the geometric and arrangement parameters of the VGs are shown in Table 4. The Reynolds number based on the chord of the airfoil is  $1 \times 10^6$ . The tunnel speed was 18.2 m/s, and the angle of attack of the airfoil experiment ranged from  $-10^\circ$  to  $25^\circ$ .

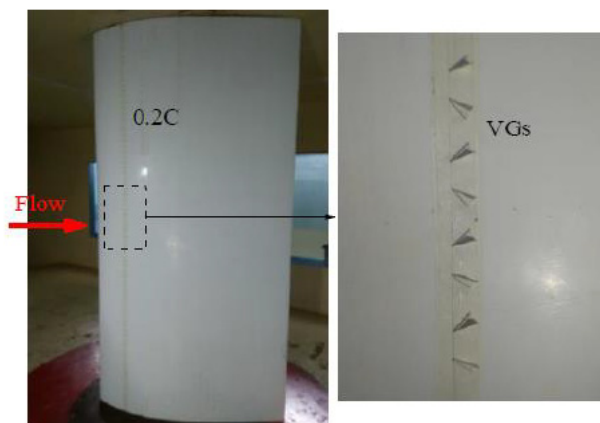


Figure 5. Test airfoil and VG geometric models.

Table 4. VG geometric parameters and arrangement.

Setting Angle $\beta$ ( $^\circ$ )	Length $l/H$	Hight $H$ (mm)	Spacing $S/H$	Pitch Distance $\lambda/H$
20	2.5	4, 6, 8	5	5

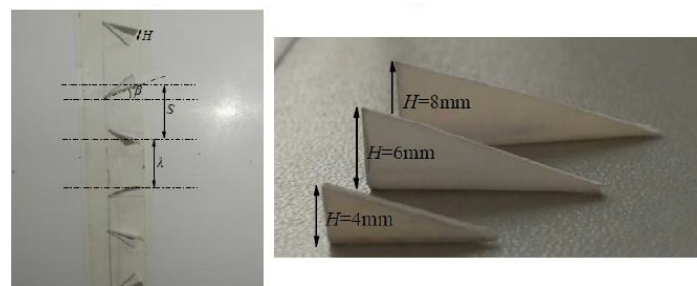


Figure 6. VG arrangement and VG height.

Figure 7 shows compares this work with that by North China Electric Power University (NCEPU), Northwest Polytechnic University (NPU), and Delft University (Delft). It can be seen that in the linear section of the lift coefficient, the experimental data achieved in this work are similar to that obtained by NPU and Delft. After airfoil stall, the lift coefficient measured in this work is the highest compared with the results of the other three works. The lift coefficient first decreases and then increases slightly. Figure 7b shows that the drag coefficient of the airfoil is low before the stall angle of attack ( $8^\circ$ ), and the drag coefficient measured in this work is similar to that measured by NPU and Delft. The drag coefficient measured after stall in this work is greater than that measured by NPU but similar to that measured by Delft. Because the aerodynamic performance of the airfoil is unstable after stall, the lift and drag coefficients have to be revised, and the mechanism of each correction method is different; however, our focus is on the aerodynamic performance before stall.

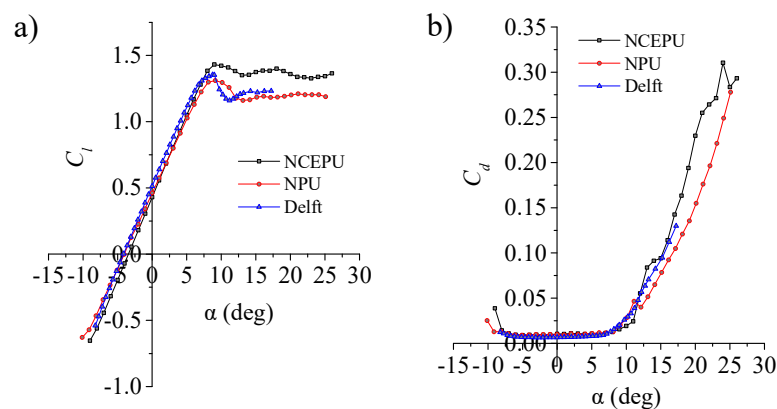


Figure 7. Comparison of experiments (a) Lift coefficient, (b) Drag coefficient.

### 3. Results and Discussion

#### 3.1. Analysis of CFD Calculation Results

Figure 8 shows the static pressure iso-contours on the leeward side of the VG. It can be seen that the low-pressure area on the leeward side of the VG appears at the middle position of the chord, and it is not generated at the leading edge of the tip. The main reason for this phenomenon is that the kinetic energy of the bottom fluid in the boundary layer is very weak because of the viscous wall. Instead of forming leading-edge separation vortices, concentrated vortices are induced when the fluid passes over the swept leading edge of the VG from the pressure surface. However, there are still low-pressure zones on the leeward side of the VG that are caused by the concentrated vortices on that side. With the increase in the height of the VG ( $H$ ) relative to the thickness of the boundary layer ( $\delta$ ), the pressure value on the leeward side of the VG is lower. The result shows that the larger the height of the VG, the greater the fluid kinetic energy in the boundary layer; thus, the concentrated vortices generated by the VG will show a stronger trend, which leads to a lower pressure in the low-pressure zone on the leeward side of the VG.

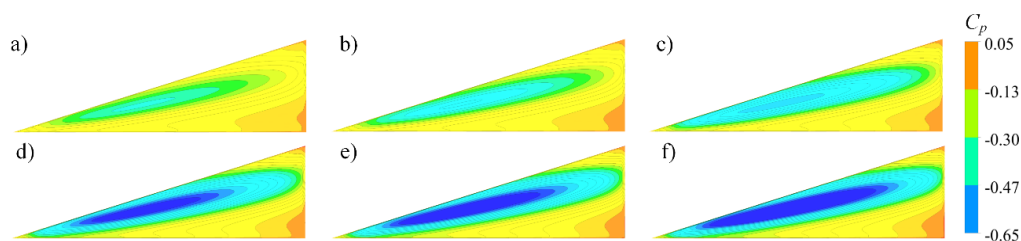


Figure 8. Static pressure iso-contours on the leeward side of the VG. (a)  $H = 0.1\delta$ , (b)  $H = 0.2\delta$ , (c)  $H = 0.5\delta$ , (d)  $H = 1.0\delta$ , (e)  $H = 1.5\delta$ , (f)  $H = 2.0\delta$ .

Figure 9 shows the distribution of the static pressure coefficient on the leeward surface of the VG; in the figure,  $S$  is the local height,  $l$  is the bottom length of the VG. Firstly, the maximum amplitude of the low-pressure coefficients occurs at about  $x = 0.4l$ , and the strongest vortex intensity can be found at  $0.4l$ . With the increase in the flow distance, the strength of the vortex core decreases gradually, and the low-pressure amplitude of the static pressure coefficient on the leeward side of the VG also presents a decreasing trend. This result shows that when the VG is placed on the wall, concentrated vortices are generated at the upper end of the VG, and the intensity of the vortices reaches the maximum value near the position  $0.4l$ . This is because the vortex gradually dissipates and is deflected away from the VG. Secondly, at any chord position, the magnitude of the static pressure coefficient increases with the increase in VG height, and the magnitudes of the static pressure coefficients are close to each other when  $H = 1.0\delta$ ,  $1.5\delta$ , and  $2.0\delta$ . When the value of  $H$  is  $0.1\delta$  and  $0.2\delta$ , the gentle pressure amplitude of the static pressure coefficient is lower, and when  $H = 0.5\delta$ , the static pressure coefficient amplitude is in the middle position.

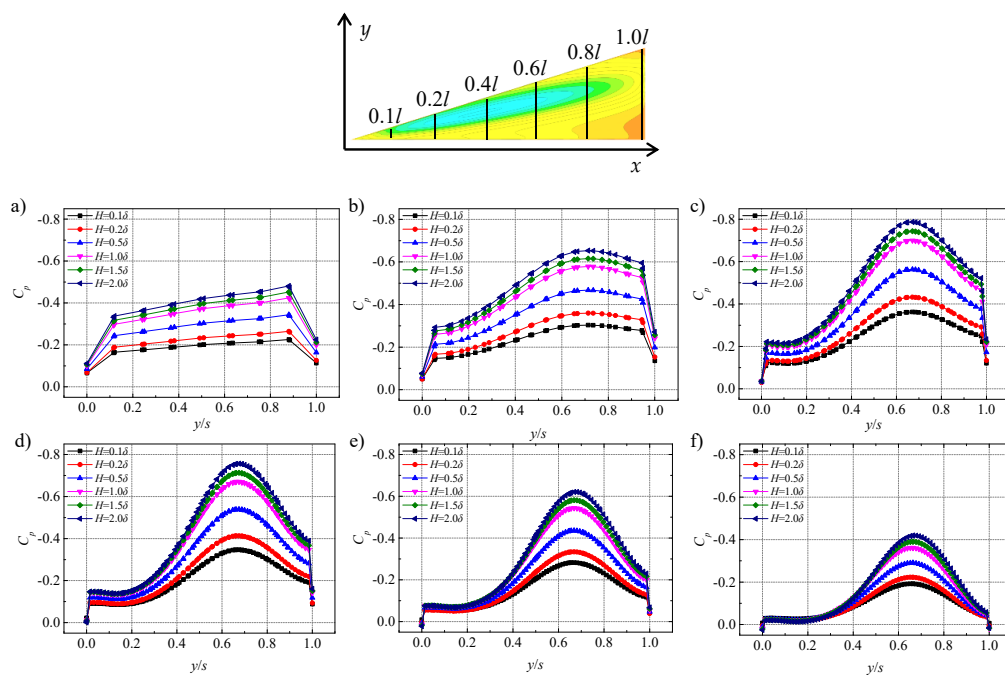


Figure 9. Distribution of static pressure coefficient on the leeward side of the VG (a)  $x = 0.1l$ , (b)  $x = 0.2l$ , (c)  $x = 0.4l$ , (d)  $x = 0.6l$ , (e)  $x = 0.8l$ , (f)  $x = 1.0l$ .

Figure 10 shows the distribution of static pressure coefficients at the center of the vortex core. It can be seen that the static pressure coefficient at the center of the vortex core first increases and then decreases in the direction of the flow and reaches the maximum at the position of  $0.5l$ . The higher the  $H$ , the lower the static pressure at the center of the vortex core.

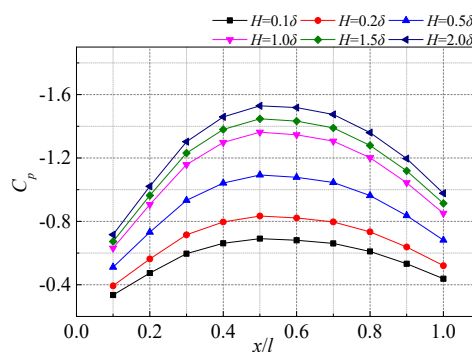


Figure 10. Distribution of static pressure coefficient at vortex core center.

Figure 11 shows the vortex core area and vortex circulation varying with the flow direction in the range of the VG surface. The area of the vortex core is almost the same at different VG heights, but it is slightly different at the trailing edge of the VG surface. The area of the vortex core is approximately exponentially distributed as the flow direction distance increases. With the increase in VG height, the vortex circulation increases gradually, and the difference becomes progressively larger as the flow becomes closer to the trailing edge of the VG.

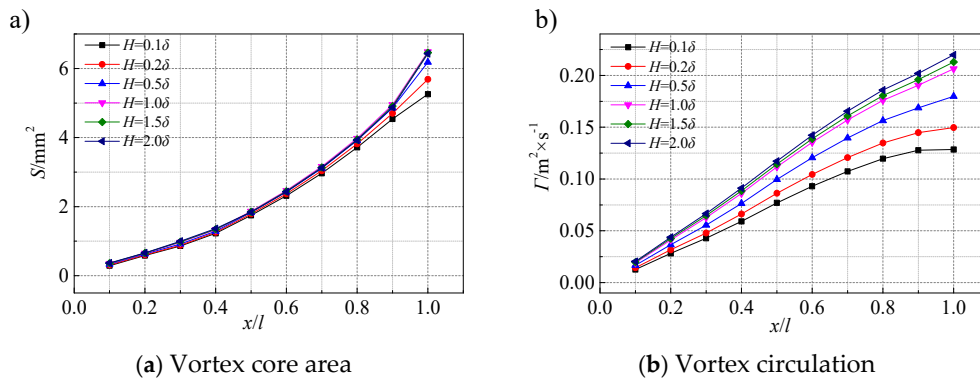


Figure 11. Chordwise distribution of vortex core area and vortex circulation.

Figure 12 shows the variation in the vortex core area and vortex circulation with the flow direction distance downstream of the VG. The area of the vortex core downstream of the VG varies linearly with the distance of the flow direction, which is slightly different from that on the VG surface. The higher the VG height, the larger the area of the vortex core, and the vortex core area difference downstream of the VG is more pronounced. However, the variation in the core circulation in the downstream direction along the VG approximately exponentially dissipates, which is very different from that on the VG surface. It can be seen that the maximum position of the VG vorticity appears at the trailing edge of the VG.

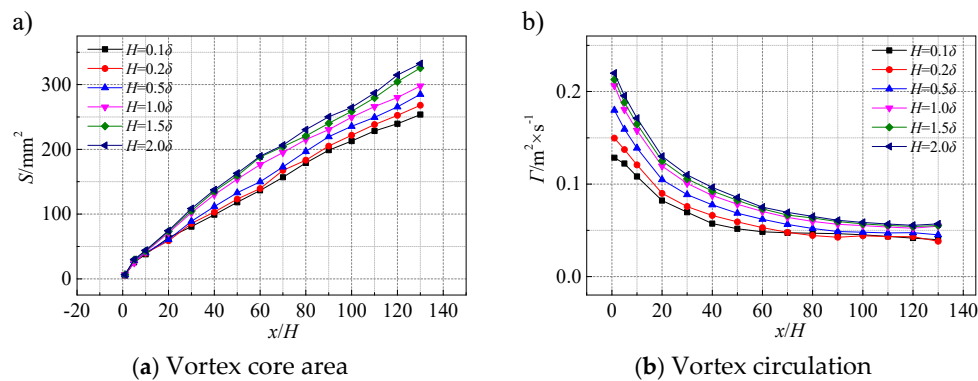
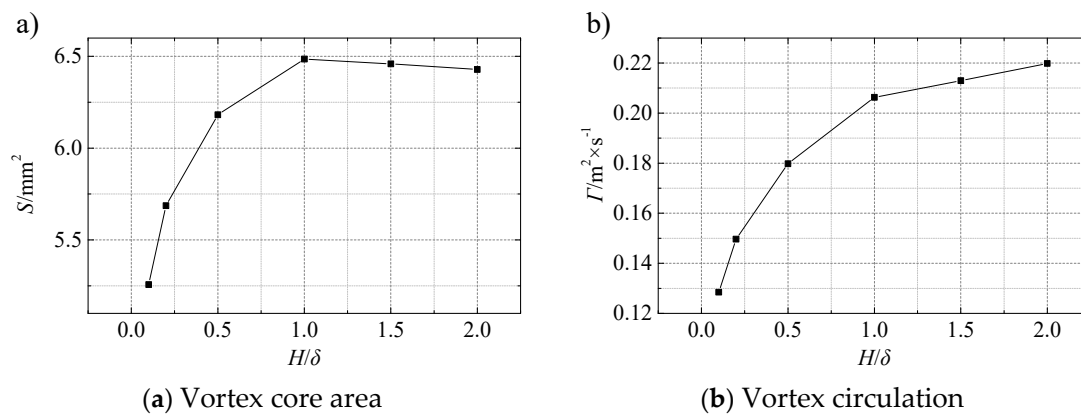


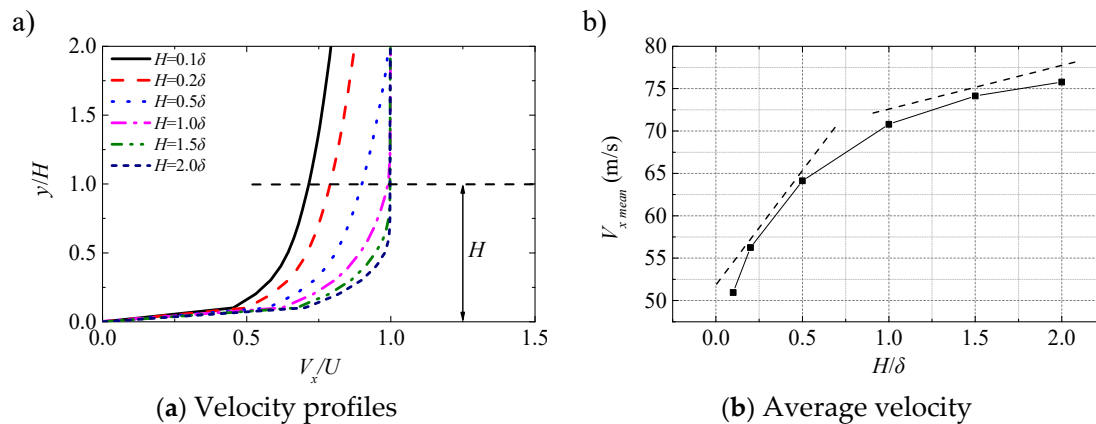
Figure 12. Distribution of vortex core area and vortex circulation with flow direction.

Figure 13 shows the variation in the vortex core area and vortex circulation as VG height increases at its trailing edge. It is shown that the vortex core area is the largest when  $H/\delta = 1.0$ . The area of the vortex core decreases slightly when  $H/\delta > 1.0$  and increases rapidly when  $H/\delta < 1.0$ . Vortex circulation is proportional to VG height: with the increase in VG height, the vortex circulation increases gradually, but it does not possess a linear relationship with VG height as it increases. When  $H/\delta < 1.0$ , the slope of vortex circulation increases when VG height is larger, but when  $H/\delta > 1.0$ , the slope of vortex circulation increases as VG height decreases.



**Figure 13.** Change in vortex core area and vortex circulation at the VG trailing edge.

Figure 14a shows the velocity profiles in the boundary layer of the inflow, and Figure 14b shows the average velocity of the fluid in the range of VG height. From Figure 14a, when the VG is in boundary layers with different thicknesses and velocity profiles of the inflow, the kinetic energy of the fluid in the boundary layer becomes progressively lower within the VG height range as the height of the boundary layer increases. It can also be seen from Figure 14b that with the increase in VG height, i.e., the decrease in the thickness of the boundary layer, the average velocity of the fluid in the VG height range becomes increasingly higher. The increase in average velocity is exponentially distributed with the height of the VG. When  $H/\delta < 1$ , the slope of average velocity in the boundary layer increases as the height of the VG presents a larger trend; after  $H/\delta > 1$ , the slope of average velocity in the boundary layer decreases with the increase in VG height.



**Figure 14.** Inflow velocity profiles and average velocity in the VG height range.

Figure 15 shows the variation in the lift, drag coefficient, and lift–drag ratio of the VG. With the increase in  $H/\delta$ , the lift coefficient of the VG increases gradually. When  $H/\delta = 2.0$ , the maximum lift coefficient of the VG is about 0.65. The drag coefficient of the VG increases with the increase in  $H/\delta$ , and the maximum drag coefficient is 0.25 when  $H/\delta = 2.0$ . The lift of the VG comes from the vortex-induced lift, and the drag is primarily pressure drag, that is, the profile drag of the VG. The variation in the lift coefficient and drag coefficient with the increase in  $H/\delta$  basically shows the same trend. The dynamic energy of the fluid in VG height, vortex circulation, lift coefficient, and drag coefficient are essentially consistent with the variation in  $H/\delta$ . The result shows that the vortex strength and drag of VG vortices are closely related to the  $H/\delta$  value, and the greater the height of the VG, the less obvious the change effect. The lift–drag ratio of the VG reaches the maximum at  $H/\delta = 0.5$ . It would be advisable to have a vorticity with a certain intensity to control the flow, but the profile

drag is not too large. However, whether the ratio of  $H/\delta$  is optimal should be discussed in relation to the kinetic energy of the fluid in the boundary layer.

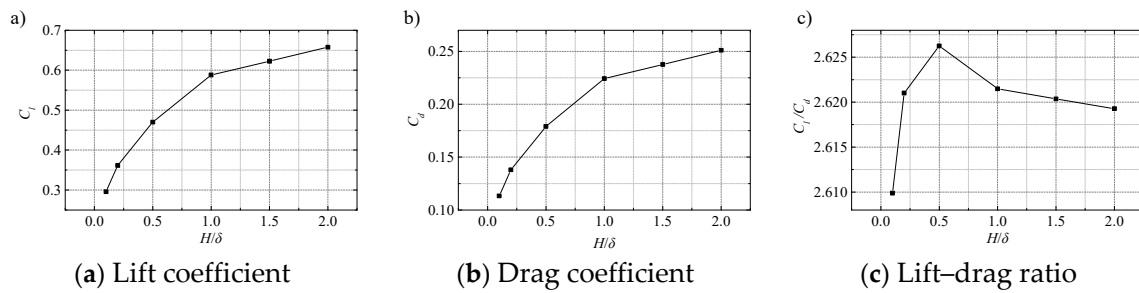


Figure 15. Lift and drag coefficient and lift–drag ratio with VG.

Figure 16 shows the axial velocity contours in different flow directions downstream of the VG. The kinetic energy of the fluid in the vortex core height is ineffective when the value of  $H/\delta$  is small. The high-energy fluid outside the vortex core is contained in the bottom layer of the boundary layer from the rotation of concentrated vortices when VG is used for flow control. From the axial velocity contours, it can be seen that with the rotation of the vortex core, the fluid kinetic energy outside the vortex core decreases, while the fluid’s streamwise kinetic energy inside the vortex core increases.

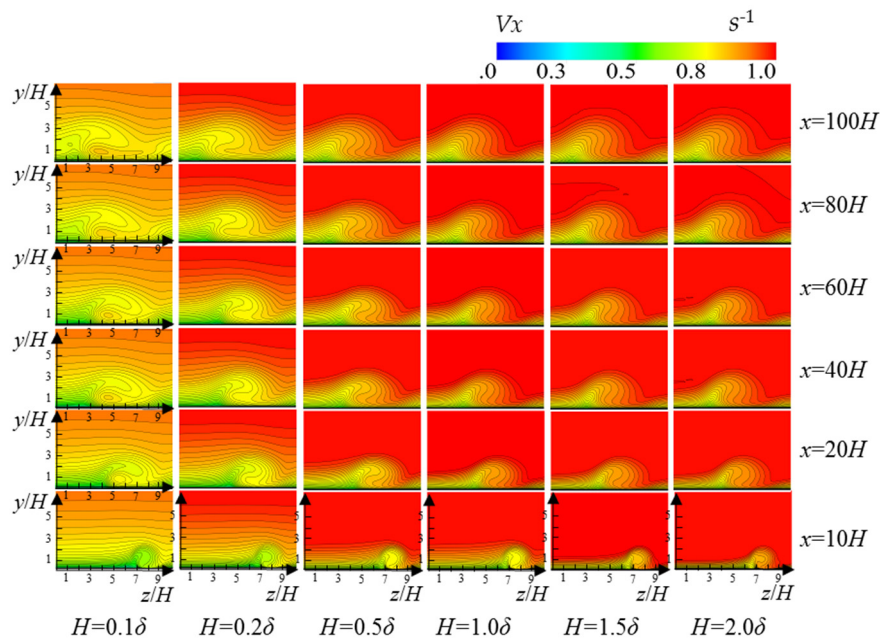


Figure 16. Axial velocity contours downstream of the VG.

Figure 17 shows the axial velocity distribution for the normal height at the vortex core position downstream of the VG. The horizontal line is placed at the center of the vortex core. With the increase in the flow distance, the area of the vortex core varies at different VG heights. The height of the vortex core marked in the figure is the height of the vortex core when  $H = 1.0\delta$ .

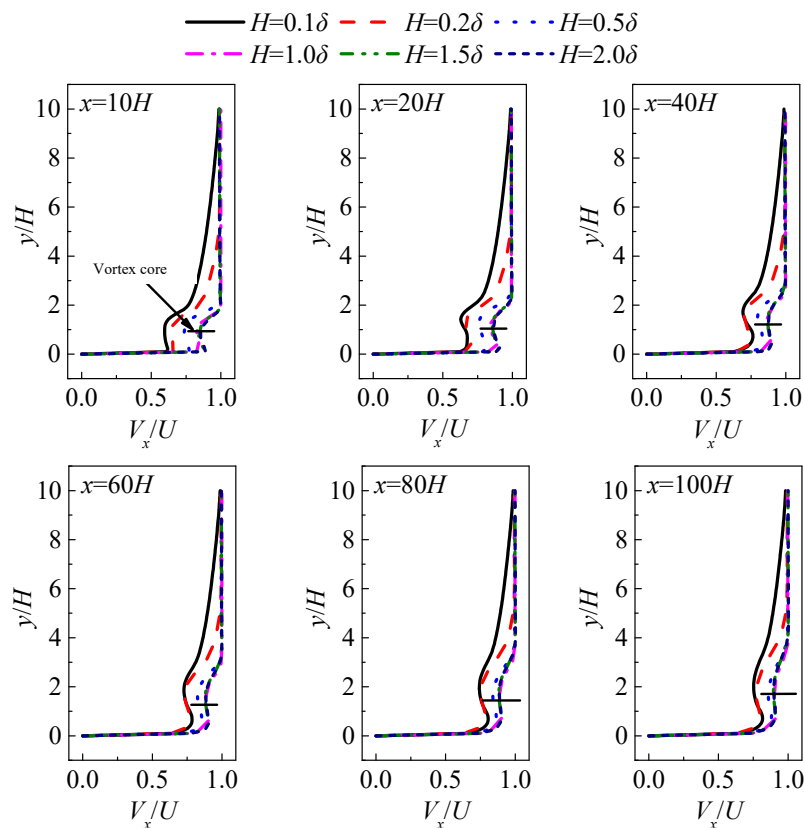


Figure 17. Velocity profiles at the vortex core downstream of the VG.

Table 5 shows the relative increase in near-wall ( $y/H < 1$ ) momentum for different VGs. Firstly, it can be observed that the center height of the vortex core increases with the increase in the flow direction distance. Secondly, the velocity profiles in the boundary layer are basically distributed in an S-line along the center of the vortex core, and the increase in fluid kinetic energy inside the vortex core corresponds to the decrease in fluid kinetic energy outside. From Table 5, comparing the kinetic energy of the bottom fluid of the boundary layer at different  $H/\delta$  values, it can be seen that the kinetic energy for the bottom fluid of the boundary layer is the lowest when  $H = 0.1\delta$  and  $0.2\delta$ , and there is little difference between them. When  $H = 0.5\delta$ , the value is intermediate; when  $H = 1.0\delta$ ,  $1.5\delta$ , and  $2.0\delta$ , the values are almost the same, and the curves basically coincide. This result shows that the kinetic energy of the fluid in the boundary layer remains largely unchanged with the increase in VG height. However, the profile drag increases with the increase in VG height, as shown in Figure 15. For flow control, it is hoped that VG can generate concentrated vortices with sufficient intensity to increase the fluid kinetic energy in the boundary layer, and this will not increase the drag of the boundary layer by much. In terms of the increasing fluid kinetic energy in the boundary layer, the value of  $H = 1.0\delta$  is the best choice.

Table 5. Relative increase in near-wall ( $y/H < 1$ ) momentum for different VGs.

Case	$x = 10H$	$x = 20H$	$x = 40H$	$x = 60H$	$x = 80H$	$x = 100H$
Clean	0%	0%	0%	0%	0%	0%
$H = 0.1\delta$	4.3%	4.1%	3.7%	3.3%	3.3%	3.3%
$H = 0.2\delta$	8.7%	4.5%	3.7%	3.3%	3.3%	3.3%
$H = 0.5\delta$	25.4%	23.7%	21.5%	19.6%	16.2%	15.5%
$H = 1.0\delta$	34.1%	32.8%	31.1%	28.4%	25.5%	24.6%
$H = 1.5\delta$	34.1%	32.8%	31.1%	28.4%	25.5%	24.6%
$H = 2.0\delta$	34.1%	32.8%	31.1%	28.4%	25.5%	24.6%

### 3.2. Analysis of Experimental Results

The results of CFD calculation show that when the VG height is about  $1.0\delta$ , the fluid kinetic energy in the near-wall basically reaches the maximum, and as the VG height continues to increase, the kinetic energy remains virtually unchanged. The experimental design was guided by CFD calculation results. The thickness of the BL of the airfoil is different at different angles of attack. To quantify the relationship between VG height and BL thickness, the airfoil was computed using Xfoil; the thickness of the BL at the VG installation position is about 5.9 mm when the maximum lift coefficient angle of attack ( $8^\circ$ ) of the airfoil is reached. Considering the machining accuracy of VGs, three VGs were designed with different heights: 4 mm, 6 mm, and 8 mm. The ratio of VG height to BL thickness is  $0.66\delta$ ,  $1.0\delta$ , and  $1.33\delta$ , respectively.

Figure 18 shows the lift coefficient, drag coefficient, and lift–drag ratio of the airfoil with and without the VG airfoils. Table 5 shows the relative variation in  $C_l$ ,  $C_d$ , and lift–drag ratio. Before the stall angle of attack ( $8^\circ$ ), the lift coefficients for the airfoil with VGs and without VGs (clean) are similar to each other in the linear section; after the  $8^\circ$  angle of attack, the lift coefficient of the airfoil without VGs remains basically unchanged, while the lift coefficient of the airfoil with VGs continues to increase. The stall angle of the clean airfoil is  $8^\circ$ , while that of the airfoil with VGs is  $18^\circ$ , so there is a  $10^\circ$  increase in the stall angle of the airfoil. When the angle of attack reaches  $23^\circ$ , the separation position of the clean airfoil is located upstream of  $0.2C$  (VG installation position), and the VGs cannot control the flow separation, so the lift coefficient of the airfoil with VGs is no different from that of the clean airfoil. The comparison of the differences among the three VG heights shows that the maximum lift coefficient of the airfoil with VGs increases by 42.8% compared with that of the clean airfoil when  $H = 0.66\delta$ ; when  $H = 1.0\delta$  and  $1.33\delta$ , the maximum lift coefficient increases by 48.7% and 48.6%, respectively. From the analysis of the maximum lift coefficient, it can be found that the VG flow control effect is the best when  $H = 1.0\delta$ .

From Figure 18b and Table 6, it can be seen that the drag coefficient for  $H = 1.33\delta$  is larger before the  $8^\circ$  angle of attack. However, beyond the  $8^\circ$  angle of attack, the drag coefficient of the clean airfoil increases rapidly. For this VG height, the drag coefficient of the airfoil with VGs is much smaller than that of the clean airfoil. With respect to the difference among the three VG heights, before the angle of attack of  $18^\circ$ , the drag coefficient of the airfoil with  $H = 1.33\delta$  is the largest, while the drag coefficients for the other two VG Heights do not much differ. The drag coefficient of the airfoil with  $H = 0.66\delta$  is 84.9% lower than that of the clean airfoil; when  $H = 1.0\delta$ , the drag coefficient of the airfoil decreases by 83.2%; when  $H = 1.33\delta$ , the drag coefficient of the airfoil decreases by 76.8%. So, among these three heights, the drag coefficient of the airfoil with  $H = 0.66\delta$  is reduced the most because the VG height is lower, and the profile drag of the VGs is minimum.

For the lift–drag ratio of the airfoil, the maximum lift–drag ratio of the clean airfoil is the highest, while the maximum lift–drag ratio of the airfoil with VGs is decreased. Therefore, the VGs cannot increase the maximum lift–drag ratio of the airfoil, but raising the angle of attack produces the best lift–drag ratio for the airfoil. The lift–drag ratio of the airfoil with VGs is larger than that of the clean airfoil after the angle of attack of  $10^\circ$ . Compared with the maximum lift–drag ratio of the airfoil with and without VGs, the maximum lift–drag ratio of the airfoil with  $H = 0.66\delta$  is 19.7% lower than that of the clean airfoil; the maximum lift–drag ratio of the airfoil with  $H = 1.0\delta$  and  $1.33\delta$  is decreased by 19.3% and 51.2%, respectively. However, when the angle of attack is  $18^\circ$  (stall angle of the airfoil with VGs), the lift–drag ratio of the airfoil with  $H = 0.66\delta$  increases by 880.3% compared with that of the clean airfoil; the lift–drag ratio increases by 821.8% when  $H = 1.0\delta$ ; and the lift–drag ratio increases by 564.8% when  $H = 1.33\delta$ . So, in summary, if considering increases in the lift coefficient and the lift–drag ratio,  $H = 1.0\delta$  has a good effect on controlling airfoil flow separation. If considering the optimal lift–drag ratio,  $H = 0.66\delta$  can meet the requirements.

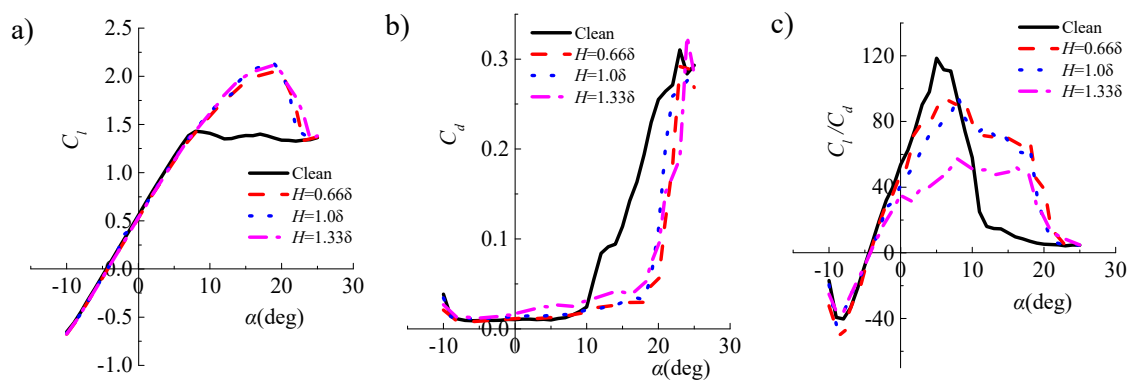


**Figure 18.** Lift coefficient, drag coefficient, and lift–drag ratio of airfoils with and without VGs. (a) Lift coefficient, (b) Drag coefficient, (c) Lift–drag ratio.

**Table 6.** Relative variation of  $C_l$ ,  $C_d$ , and lift–drag ratio.

Case	Stall Attack Angle	Increment of Maximum $C_l$	Decrease of $C_d$ at $18^\circ$	Decrease of Maximum Lift–Drag Ratio	Increment of Lift–Drag Ratio at $18^\circ$
Clean	$8^\circ$	0%	0%	0%	0%
$H = 0.66\delta$	$18^\circ$	42.8%	84.9%	19.7%	880.3%
$H = 1.0\delta$	$18^\circ$	48.7%	83.2%	19.3%	821.8%
$H = 1.33\delta$	$18^\circ$	48.6%	76.8%	51.2%	564.8%

Figure 19 shows the static pressure coefficient ( $C_p$ ) distribution on the airfoil surface at different angles of attack. The pressure taps are located on the pressure side of the two VGs, so the  $C_p$  curve will be prominently downward near the installation locations of the VGs. The  $C_p$  curves of the airfoil with and without VGs are similar to each other at  $0^\circ$  and  $5^\circ$  angles of attack, and there are no differences among the three VG heights. A pressure plateau appears on the  $C_p$  curve of the clean airfoil about  $88H$  away from the installation position of the VGs when the angle of attack is  $10^\circ$ . The reverse pressure gradient of the clean airfoil is about  $-0.77$  kpa/m; with the action of the VGs, the pressure plateau on the  $C_p$  curve for the airfoil with VGs disappears, and the  $C_p$  curves do not differ among the three VG heights. With the increase in the angle of attack, the separation position of the clean airfoil is closer to the installation position of the VGs, and this configuration is beneficial to the control flow separation by the VGs when the angle of attack is  $15^\circ$ ,  $18^\circ$ , and  $20^\circ$ . However, with the increase in the angle of attack, the reverse pressure gradient for the clean airfoil becomes progressively larger. Therefore, with the increase in the angle of attack, the VGs cannot completely inhibit the flow separation, although they can postpone it.

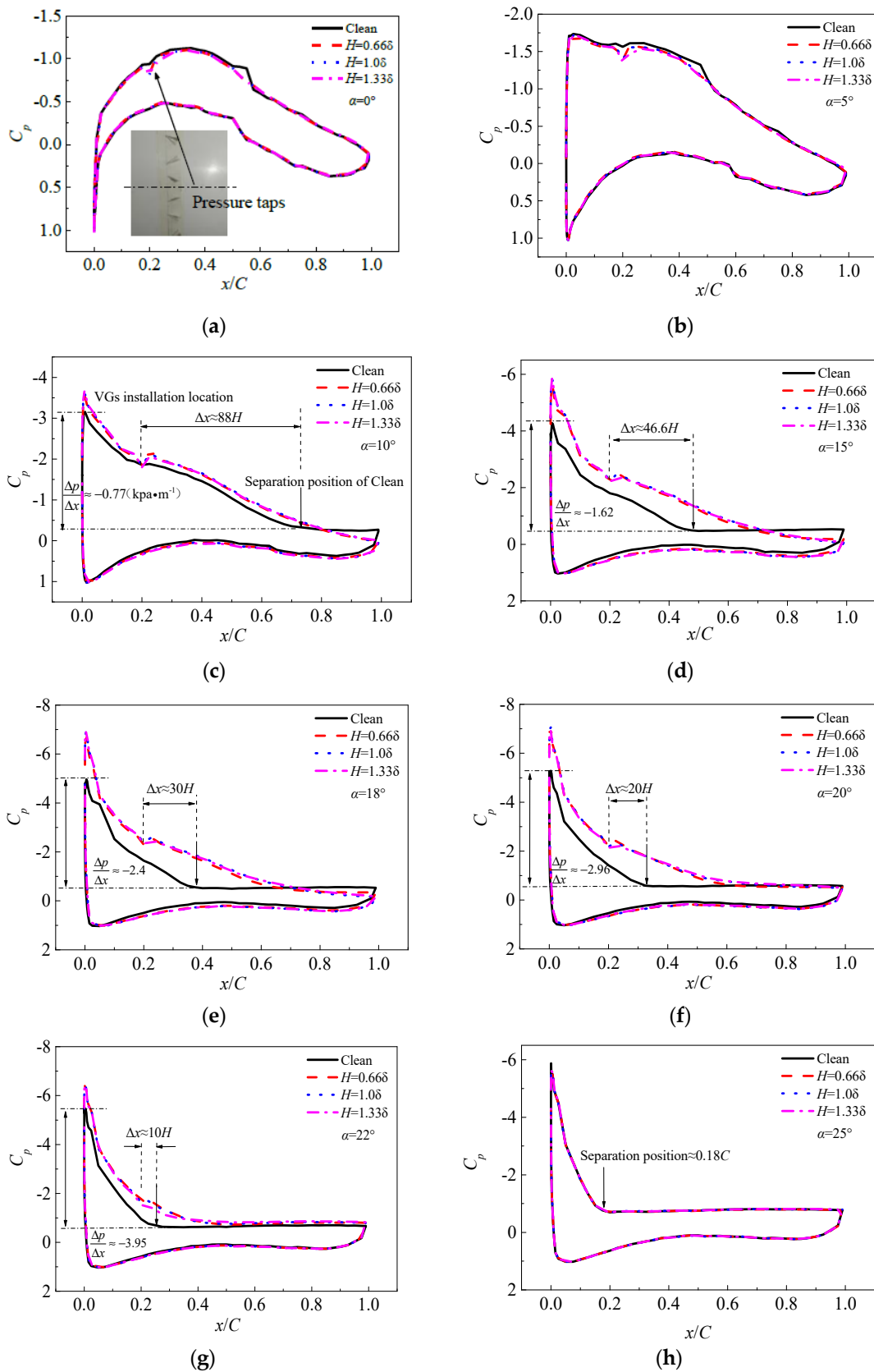


**Figure 19.** Distribution of  $C_p$  on the airfoil surface. (a)  $\alpha = 0^\circ$ , (b)  $\alpha = 5^\circ$ , (c)  $\alpha = 10^\circ$ , (d)  $\alpha = 15^\circ$ , (e)  $\alpha = 18^\circ$ , (f)  $\alpha = 20^\circ$ , (g)  $\alpha = 22^\circ$ , (h)  $\alpha = 25^\circ$ .

The separation position of the airfoil is very close to the installation positions of the VGs, and the reverse pressure gradient is further increased where a large pressure plateau appears on the  $C_p$  curve for the airfoil with VGs when the angle of attack is  $22^\circ$ . In this scenario ( $22^\circ$  angle of attack), the amplitude of the  $C_p$  curve is slightly lower at  $H = 1.33\delta$ , and the position of the pressure plateau appears earlier than for the other two VG heights. When the angle of attack is  $25^\circ$ , because the flow separation of the clean airfoil has been occurring upstream of the VGs, the  $C_p$  curve of the airfoil with VGs coincides with that of the clean airfoil.

Figure 20 shows the distribution of the total pressure coefficient of the wake rake. It can be seen that the total pressure loss of the airfoil with VGs is higher than that of the clean airfoil at  $0^\circ$ ,  $5^\circ$ , and  $10^\circ$  angles of attack. The total pressure loss for  $H = 1.33\delta$  is higher than that for the other two VG heights at the  $5^\circ$  and  $10^\circ$  angles of attack. The total pressure loss of the airfoil with VGs is obviously smaller than that of the clean airfoil at  $15^\circ$  and  $18^\circ$  angles of attack; in this case, there is little difference among the three VG heights. The total pressure loss of the airfoil with VGs is still less than that of the clean airfoil at  $20^\circ$  and  $22^\circ$  angles of attack, for which the total pressure loss is the smallest when  $H = 0.66\delta$ , and there is little difference between the other two VG heights. The total pressure coefficient curves of the airfoils with VGs coincide with that of the clean airfoil when the angle of attack is  $25^\circ$ .

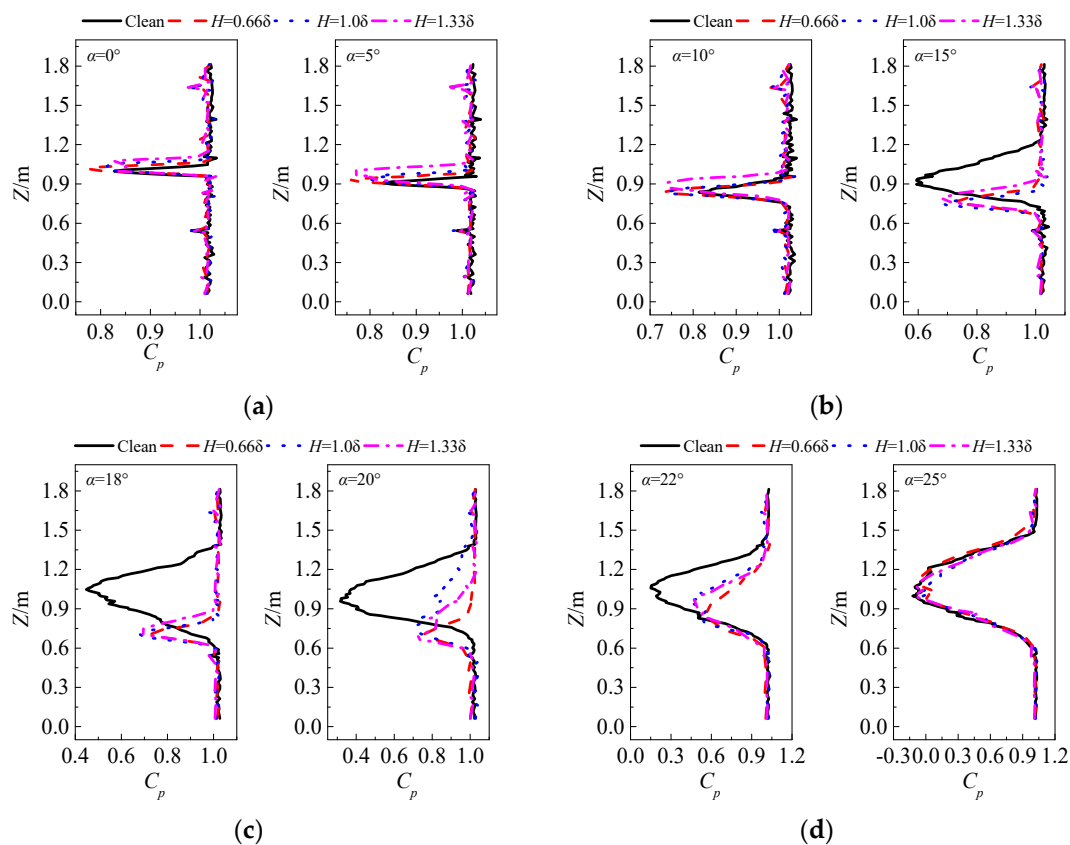


**Figure 20.** Distribution of total pressure coefficient at the wake rake. (a)  $\alpha = 0^\circ$ ;  $5^\circ$ , (b)  $\alpha = 10^\circ$ ;  $15^\circ$ , (c)  $\alpha = 18^\circ$ ;  $20^\circ$ , (d)  $\alpha = 22^\circ$ ;  $25^\circ$ .

#### 4. Conclusions

When VGs are used for flow control, they are often put on the surface of an object. The characteristics of the vortices generated by VGs are quite different from those of aeronautical delta wings. The VGs are located on the surface of the object, and the concentrated vortices are not generated at the leading edge of the tip; instead, the fluid flows from the windward side of the VGs to the leeward surface, forming a concentrated vortex on the leeward side, and the intensity of the vortex reaches the maximum at the trailing edge of the VGs. There is a logarithmic relationship between the

vortex circulation and VG height, and the average kinetic energy of the fluid in the boundary layer also has a logarithmic relationship with the VG height, so the vortex intensity of the VGs is proportional to the average kinetic energy of the fluid in the boundary layer. The greater the height of the VGs, the stronger the intensity of the concentrated vortices, and the stronger the flow control ability, but the greater the profile drag produced by the VGs. The lift and drag of the VG basically have a logarithmic relationship with the height of the VGs, but the lift–drag ratios of the VGs are not the same. The VG lift–drag ratio is the largest when  $H = 0.5\delta$ . In this case, the VG height can be well balanced with the concentrated vortex intensity and profile drag. The fluid kinetic energy in the boundary layer is the lowest when  $H = 0.1\delta$  and  $0.2\delta$ , and there is little difference between them; it is second lowest when  $H = 0.5\delta$ ; and the fluid kinetic energy in the boundary layer is the highest with coinciding curves when  $H = 1.0\delta$ ,  $1.5\delta$ , and  $2.0\delta$ . This shows that when the height of the VG increases, the fluid kinetic energy in the boundary layer is basically unchanged, but the profile drag increases with the height of the VGs. For flow control, it is hoped that VGs can generate a vortex of sufficient intensity to increase the fluid kinetic energy in the boundary layer and that the profile drag will not increase too much. On this basis,  $H = 1.0\delta$  is the better height.

From the results of wind tunnel experiments, the stall angle of the airfoil without VGs is  $8^\circ$  and that of the airfoil with VGs is  $18^\circ$ , so VGs increase the stall angle of the airfoil by  $10^\circ$ . The maximum lift coefficient increases by 42.8% relative to the airfoil without VGs when  $H = 0.66\delta$ ; it increases by 48.7% when  $H = 1.0\delta$ ; and it increases by 48.6% when  $H = 1.33\delta$ . So, at the maximum lift coefficient, the VG flow control effect is the best when  $H = 1.0\delta$ .

Before the stall angle of the airfoil without VGs, VGs increase the drag and decrease the lift–drag ratio of the airfoil; after the stall angle, it can decrease the drag and increase the lift–drag ratio of the airfoil. The drag coefficient of the airfoil with VGs is 84.9% lower than that of the airfoil without VGs when  $H = 0.66\delta$ ; it decreases by 83.2% when  $H = 1.0\delta$  and decreases by 76.8% when  $H = 1.33\delta$ . The drag coefficient of the airfoil decreases most when  $H = 0.66\delta$ , indicating that the height of the VGs is low and the airfoil drag is minimum. The maximum lift–drag ratio of the airfoil without VGs is the highest, while the maximum lift–drag ratio of the airfoil with VGs decreases. So, VGs do not increase the maximum lift–drag ratio of the airfoil, but VGs increase the angle of attack of the best lift–drag ratio of the airfoil. The lift–drag ratio of the airfoil with VGs is larger than that of the airfoil without VGs after an angle of attack of  $10^\circ$ . When the angle of attack of the airfoil is  $18^\circ$ , the lift–drag ratio of the airfoil with VGs increases by 880.3% when  $H = 0.66\delta$ , by 821.8% when  $H = 1.0\delta$ , and by 564.8% when  $H = 1.33\delta$ . So, in summary, for the choice of VG height, if aiming to increase the lift coefficient and the lift–drag ratio,  $H = 1.0\delta$  has a good effect. If considering the optimal lift–drag ratio,  $H = 0.66\delta$  can meet the requirements.

**Author Contributions:** X.L., K.Y., X.W. conceived the research idea. X.L., X.W. performed numerical simulation. X.L., X.W. analyzed data and numerical results. All authors have contributed to the writing, editing, and revising of this manuscript.

**Funding:** This work was jointly supported by the National Natural Science Foundation of China (51806221), the National Natural Science Foundation of China (51705498).

**Conflicts of Interest:** The authors declare no conflict of interest.

## References

1. Council GWE. *GWEC Global Wind Report 2017*; Global Wind Energy Council: Bonn, Germany, 2017.
2. Khamlaj, T.A.; Rumpfkeil, M.P. Analysis and optimization of ducted wind turbines. *Energy* **2018**, *162*, 1234–1252. [[CrossRef](#)]
3. Wang, Y.; Li, G.; Shen, S.; Huang, D.; Zheng, Z.C. Influence of an off-surface small structure on the flow control effect on horizontal axis wind turbine at different relative inflow angles. *Energy* **2018**, *160*, 101–121. [[CrossRef](#)]
4. Ebrahimi, A.; Movahhedi, M. Wind turbine power improvement utilizing passive flow control with microtab. *Energy* **2018**, *150*, 575–582. [[CrossRef](#)]

5. Moshfeghi, M.; Shams, S.; Hur, N. Aerodynamic performance enhancement analysis of horizontal axis wind turbines using a passive flow control method via split blade. *J. Wind Eng. Ind. Aerodyn.* **2017**, *167*, 148–159. [[CrossRef](#)]
6. Ebrahimi, A.; Movahhedi, M. Power improvement of NREL 5-MW wind turbine using multi-DBD plasma actuators. *Energy Convers. Manag.* **2017**, *146*, 96–106. [[CrossRef](#)]
7. Lin, J.C. Review of research on low-profile vortex generators to control boundary-layer separation. *Prog. Aerosp. Sci.* **2002**, *38*, 389–420. [[CrossRef](#)]
8. Macquart, T.; Maheri, A.; Busawon, K. Microtab dynamic modelling for wind turbine blade load rejection. *Renew. Energy* **2014**, *64*, 144–152. [[CrossRef](#)]
9. Kametani, Y.; Fukagata, K.; Orlu, R.; Schlatter, P. Effect of uniform blowing/suction in a turbulent boundary layer at moderate Reynolds number. *Int. J. Heat Fluid Flow* **2015**, *55*, 132–142. [[CrossRef](#)]
10. Ziadé, P.; Feero, M.A.; Sullivan, P.E. A numerical study on the influence of cavity shape on synthetic jet performance. *Int. J. Heat Fluid Flow* **2018**, *74*, 187–197. [[CrossRef](#)]
11. Yang, H.; Jiang, L.-Y.; Hu, K.-X.; Peng, J. Numerical study of the surfactant-covered falling film flowing down a flexible wall. *Eur. J. Mech. Fluids* **2018**, *72*, 422–431. [[CrossRef](#)]
12. Abdollahzadeh, M.; Pascoa, J.C.; Oliveira, P.J. Comparison of DBD plasma actuators flow control authority in different modes of actuation. *Aerospace Sci. Technol.* **2018**, *78*, 183–196. [[CrossRef](#)]
13. Barlas, T.K.; van Kuik, G.A.M. Review of state of the art in smart rotor control research for wind turbines. *Prog. Aerospace Sci.* **2010**, *46*, 1–27. [[CrossRef](#)]
14. Johnson, S.J.; Baker, J.P.; Dam, C.P.V. An overview of active load control techniques for wind turbines with an emphasis on microtabs. *Wind Energy* **2010**, *13*, 239–253. [[CrossRef](#)]
15. Wang, H.; Zhang, B.; Qiu, Q.; Xu, X. Flow control on the NREL S809 wind turbine airfoil using vortex generators. *Energy* **2017**, *118*, 1210–1221. [[CrossRef](#)]
16. Taylor, H.D. *The Elimination of Diffuser Separation by Vortex Generators*; United Aircraft Corporation: Moscow, Russia, 1947.
17. Manolesos, M.; Voutsinas, S.G. Experimental investigation of the flow past passive vortex generators on an airfoil experiencing three-dimensional separation. *J. Wind Eng. Ind. Aerodyn.* **2015**, *142*, 130–148. [[CrossRef](#)]
18. Gao, L.; Zhang, H.; Yongqian, L.; Han, S. Effects of vortex generators on a blunt trailing-edge airfoil for wind turbines. *Renew. Energy* **2015**, *76*, 303–311. [[CrossRef](#)]
19. Afjeh, A.A.; Keith, T.G.; Fateh, A. Predicted aerodynamic performance of a horizontal-axis wind turbine equipped with vortex generators. *J. Wind Eng. Ind. Aerodyn.* **1990**, *33*, 515–529. [[CrossRef](#)]
20. Hu, J.; Wang, R.; Huang, D. Flow control mechanisms of a combined approach using blade slot and vortex generator in compressor cascade. *Aerosp. Sci. Technol.* **2018**, *78*, 320–331. [[CrossRef](#)]
21. Grébert, A.; Bodart, J.; Jamme, S.; Laurent, J. Simulations of shock wave/turbulent boundary layer interaction with upstream micro vortex generators. *Int. J. Heat Fluid Flow* **2018**, *72*, 73–85. [[CrossRef](#)]
22. Urkiola, A.; Fernandez-Gamiz, U.; Errasti, I.; Zulueta, E. Computational characterization of the vortex generated by a Vortex Generator on a flat plate for different vane angles. *Aerosp. Sci. Technol.* **2017**, *65*, 18–25. [[CrossRef](#)]
23. Oneissi, M.; Habchi, C.; Russeil, S.; Lemenand, T.; Bougeard, D. Heat transfer enhancement of inclined projected winglet pair vortex generators with protrusions. *Int. J. Therm. Sci.* **2018**, *134*, 541–551. [[CrossRef](#)]
24. Mondal, B.; Lopez, C.F.; Verma, A.; Mukherjee, P.P. Vortex generators for active thermal management in lithium-ion battery systems. *Int. J. Heat Mass Trans.* **2018**, *124*, 800–815. [[CrossRef](#)]
25. Godard, G.; Stanislas, M. Control of a decelerating boundary layer. Part 1: Optimization of passive vortex generators. *Aerosp. Technol.* **2006**, *10*, 181–191. [[CrossRef](#)]
26. Godard, G.; Stanislas, M. Control of a decelerating boundary layer. Part 2: Optimization of slotted jets vortex generators. *Aerosp. Sci. Technol.* **2006**, *10*, 394–400. [[CrossRef](#)]
27. Godard, G.; Stanislas, M. Control of a decelerating boundary layer. Part 3: Optimization of round jets vortex generators. *Aerosp. Sci. Technol.* **2006**, *10*, 455–464. [[CrossRef](#)]
28. Velte, C.M. *Characterization of Vortex Generator Induced Flow*; Technical University of Denmark: Copenhagen, Denmark, 2009.
29. Angele, K.P.; Grewe, F. Instantaneous Behavior of Streamwise Vortices for Turbulent Boundary Layer Separation Control. *J. Fluid. Eng.* **2007**, *129*, 226–235. [[CrossRef](#)]

30. Sørensen, N.N.; Zahle, F.; Bak, C.; Vronsky, T. Prediction of the Effect of Vortex Generators on Airfoil Performance. *J. Phys. Conf. Ser.* **2014**, *524*, 12–19. [[CrossRef](#)]
31. Mueller-Vahl, H.P.G.; Nayeri, C.N.; Paschereit, C.O. Vortex generators for wind turbine blades: A combined wind tunnel and wind turbine parametric study. In Proceedings of the ASME Turbo Expo 2012: Turbine Technical Conference and Exposition, Copenhagen, Denmark, 11–15 June 2012; pp. 899–914.
32. Fouatih, O.M.; Medale, M.; Imine, O.; Imine, B. Design optimization of the aerodynamic passive flow control on NACA 4415 airfoil using vortex generators. *Eur. J. Mech. Fluids* **2016**, *56*, 82–96. [[CrossRef](#)]
33. Velte, C.M.; Hansen, M.O.L. Investigation of flow behind vortex generators by stereo particle image velocimetry on a thick airfoil near stall. *Wind Energy* **2013**, *16*, 775–785. [[CrossRef](#)]
34. Hansen, M.O.L.; Velte, C.M.; Øye, S.; Hansen, R.; Sorensen, N.N.; Mikkelsen, R. Aerodynamically shaped vortex generators. *Wind Energy* **2016**, *19*, 563–567. [[CrossRef](#)]
35. Kerho, M.; Hutcherson, S.; Blackwelder, R.F.; Liebeck, R.H. Vortex generators used to control laminar separation bubbles. *J. Aircr.* **1993**, *30*, 315–319. [[CrossRef](#)]
36. Timmer, W.A.; van Rooij, R.P.J.O.M. Summary of the Delft University Wind Turbine Dedicated Airfoils. *J. Sol. Energy Eng.* **2003**, *125*, 11–21. [[CrossRef](#)]
37. Gyatt, G.W. *Development and Testing of Vortex Generators for Small Horizontal Axis Wind Turbines*; AeroVironment Inc.: Monrovia, CA, USA, 1986.
38. Sullivan, T.L. Effect of vortex generators on the power conversion performance and structural dynamic loads of the Mod-2 wind turbine. *A.V. Samokhvalov / Physica C* **1984**, *259*, 337–348.
39. Kogaki, T.; Matsumiya, H.; Kieda, K.; Yoshimizu, N. Performance Improvement of Airfoil for Wind Turbines by the Modified Vortex Generator. *Wind Energy* **2004**, *28*, 73–76.
40. Fernandez-Gamiz, U.; Gomez-Mármol, M.; Chacón-Rebollo, T. Computational Modeling of Gurney Flaps and Microtabs by POD Method. *Energies* **2018**, *11*, 2091. [[CrossRef](#)]



© 2019 by the authors. Licensee MDPI, Basel, Switzerland. This article is an open access article distributed under the terms and conditions of the Creative Commons Attribution (CC BY) license (<http://creativecommons.org/licenses/by/4.0/>).